Escola de Primavera de Transição e Turbulência
Blumenau 2020

ABCM Associação Brasileira de Engenharia e Ciências Mecânicas

12th Spring School on Transition and Turbulence
September 21st-25th, 2020, Blumenau, SC, Brazil

EPTT-2020-0038
DYNAMIC FLOW STRUCTURES IN THE WAKE OF A SURFACE-MOUNTED FINITE-HEIGHT SQUARE PRISM

Barbara L. da Silva
David Sumner
Donald J. Bergstrom
Department of Mechanical Engineering, University of Saskatchewan
57 Campus Drive, Saskatoon, Saskatchewan, S7N 5A9, Canada
barbara.silva@usask.ca, david.sumner@usask.ca, don.bergstrom@usask.ca

Abstract. *The flow around surface-mounted finite-height square prisms is complex due to the strong three-dimensionality of the flow, especially for prisms of small aspect ratio AR = H/D (where D is the prism width and H is its height). Different flow models have been proposed in the literature to describe the dynamic flow structures in the wake of surface-mounted prisms, although gaps and inconsistencies remain – for instance, in explaining the origins of regions of high streamwise vorticity in the upper part of the wake. This study aims to explore the dynamic flow structures in the wake of a surface-mounted finite-height square prism of AR = 3 at a Reynolds number of Re = 500 based on the prism width, with a thin boundary layer on the ground plane. Large-eddy simulation results were analyzed using a phase-average approach to extract the dominant periodic features of the wake. The phase-averaged flow fields show the occurrence of alternating structures similar to half-loops, although the regions of highest streamwise vorticity take place outside the near-wake formation region and are associated with the downwash and with a large-scale motion of the wake in the transverse direction. The dynamic behavior of the wake reveals the alternate entrainment of fluid close to the ground plane. In contrast, the upper region of the wake is more symmetric.*

Keywords: *surface-mounted finite-height square prism, turbulent wake, bluff body, large-eddy simulation, phase average.*

1. INTRODUCTION

The flow around bluff bodies is found in many situations, including moving automobiles and trucks, the wind around buildings, chimneys and wind turbines, and the wind and ocean currents acting on offshore structures. In engineering applications, a common approach to facilitate the study of the flow field around complex obstacles is by approximating them to simpler geometries, such as a circular or square prism. For a prism of height H and characteristic length D, if the aspect ratio AR = H/D is very high, a two-dimensional or "infinite" assumption can be made so that the end effects of the prism are negligible. In this case, flow separation and subsequent vortex shedding are assumed to take place along the entire prism height.

The flow field and fluid forces for the infinite (two-dimensional) prism are reasonably well understood over a wide range of flow conditions (e.g. Igarashi, 1984; Ozgoren, 2006). However, for most applications, the end conditions of the prism change the flow significantly by introducing three-dimensional structures, which make the flow field and the fluid-obstacle interactions more complex. For the specific case of the cross-flow around a surface-mounted finite-height square prism, one of its ends (the junction) is attached to a ground surface, and the other end (the free end) is exposed to the flow and subject to flow separation. Some of the main flow structures of the time-averaged wake are illustrated in Fig. 1. They include the horseshoe vortex system, lateral and top recirculation regions due to the flow separation from the upstream edges of these surfaces, the top and base counter-rotating pairs of streamwise vortices (not shown in the figure), the corner vortices and a recirculation region downstream of the prism with downwash (Wang and Zhou, 2009; Sumner *et al*., 2017; Zhang *et al*., 2017; da Silva *et al*., 2020). The presence of some of the flow structures in the wake may depend on the prism AR, the relative boundary layer thickness δ/D or δ/H, and the Reynolds number Re = $U_\infty D/\nu$, where U_∞ is the freestream velocity and ν is the kinematic viscosity of the fluid. For example, the streamwise vorticity pair at the upper part of the wake is typically always present and associated with the downwash, whereas the base vortices are sometimes absent, especially for thin boundary layers (Hosseini *et al*., 2013). In this case, the wake is a dipole type. When the base vortices are present, they are usually accompanied by an upwash flow in the wake, and the wake is characterized as a quadrupole type.

Various flow models have been proposed to explain the instantaneous wake behavior of surface-mounted finite-height square prisms. The model of Sakamoto and Arie (1983) introduced a critical AR that subdivided the occurrence of

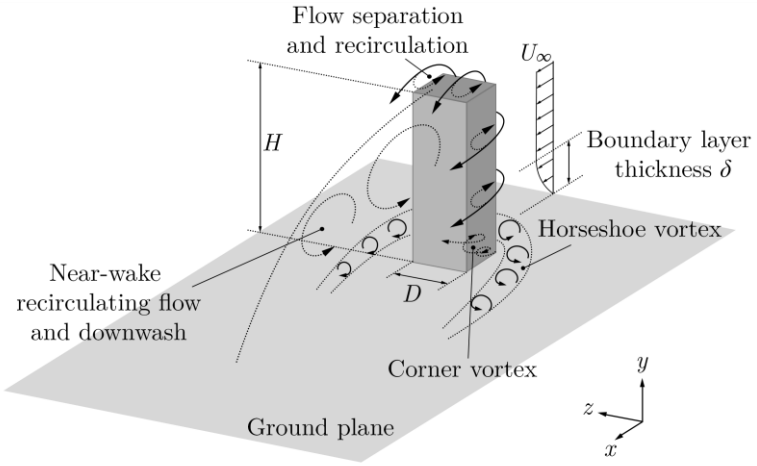

Figure 1. Schematic of the flow around a surface-mounted finite-height square prism.

different structures: above the critical AR, the near wake would present the antisymmetric von Kármán vortex shedding along the prism height, except for regions close to the free end or the prism-ground junction (Wang *et al*., 2004). Below the critical AR, an arch-type or hairpin vortex would prevail, which consists of two spanwise "legs" connected near the free end and shed in a contiguous manner from the top and lateral surfaces (Kawai *et al.*, 2012; Sakamoto and Arie, 1983). Instantaneous particle image velocimetry (PIV) measurements performed by Wang and Zhou (2009) resulted in the proposal of a different flow model, where the near-wake structure was described as an arch vortex even above the critical AR. The arch vortex was found to be shed with symmetric and antisymmetric modes, with the symmetric mode being more frequent for lower AR.

One of the main points addressed in the model of Wang and Zhou (2009) was the source of the large streamwise vorticity regions. Earlier studies like Wang *et al*. (2004) attributed the streamwise vorticity in the upper part of the wake to independent structures that were formed from the corners of the tip of the prism – hence their common name, "tip vortices". Wang and Zhou (2009), on the other hand, found the streamwise vorticity to be associated with the projection of the vertically inclined arch vortices, and therefore to be a part of the overall wake structure.

A more recent interpretation of the structures in the near wake of a surface-mounted finite-height square prism was proposed by Bourgeois *et al*. (2011), based on a phase average analysis of the dipole wake of a prism with AR = 4, also using PIV. The authors observed an always antisymmetric shedding of half-loop structures in the wake of the prism. Each half-loop consisted of an approximately vertical leg at the ground surface, resembling a Kármán vortex, connected at its top to adjacent half-loops by a mostly streamwise strand. In the case of a quadrupole wake, full loops with additional connector strands at their bases were observed instead (Hosseini *et al*., 2013).

In this flow model, the time-averaged streamwise vorticity was associated with the averaging of the connector strands of the half-loops, argued to be generated from the combination of the two other vorticity components of the flow detaching from the top and sides of the prism. However, these streamwise strands are inclined downward and shown to be connected to the base of the next half-loop. Its proximity to the ground plane is, therefore, inconsistent with the location of the large time-averaged streamwise vorticity regions. Da Silva *et al*. (2020) investigated the time-averaged wake of a surface-mounted finite-height square prism with AR = 3, and found the mean streamwise vorticity to be formed from the three-dimensional bending of the flow that encircles the near wake, caused by the downwash.

Other recent studies addressed different aspects of the dynamic wake of surface-mounted finite-height square prisms, which include the effects of the flow on wind load fluctuations (Zu and Lam, 2018), the occurrence of symmetric and antisymmetric shedding modes (Sattari *et al*., 2012; Behera and Saha, 2019), low-frequency instabilities near the free end (Kindree *et al*., 2018), the influence of the boundary layer thickness on the horseshoe vortex interaction with the wake (El Hassan *et al.*, 2015) and the occurrence of cellular shedding, which is found mostly for larger AR (Porteous *et al*., 2017; Yauwenas *et al*., 2019). However, the dynamic wake of surface-mounted finite-height square prisms is not yet fully clarified and contradictions remain about the shape of these structures, the cause of the streamwise vorticity regions, and the overall mechanism of shedding for this type of bluff body. The present study aims to address this gap in the literature, using a surface-mounted finite-height square prism with AR = 3 and Re = 500 as a reference case. The dynamic features of the wake will be investigated based on the phase-averaged flow field around the prism.

2. COMPUTATIONAL MODELS AND METHODS

A large-eddy simulation (LES) of the flow around a surface-mounted finite-height square prism was performed for the present analysis, with the dynamic Lagrangian subgrid-scale model of Meneveau et al. (1996). The prism had a width of D = 0.02 m and an aspect ratio of AR = 3. The computational domain, presented in Fig. 2a, extends 20D in the

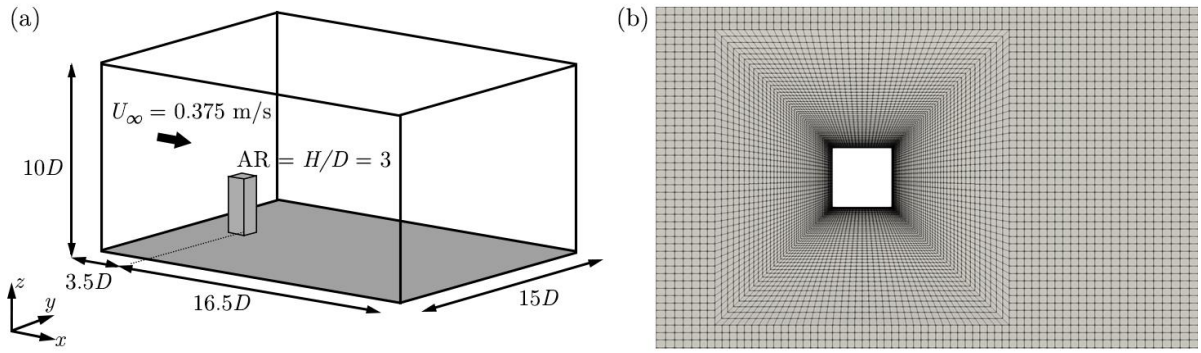

Figure 2. (a) Computational domain and (b) section of the grid near the prism in a *x*-*y* plane.

streamwise (*x*) direction, 15*D* in the transverse (*y*) direction and 10*D* in the vertical (*z*) direction, with the inlet boundary located 3.5*D* upstream of the prism center. The origin of the computational domain is located at the center of the base of the prism.

A uniform speed of 0.375 m/s was prescribed for the inlet, which gave a Reynolds number Re = 500 and a relative boundary layer thickness of $\delta/D = 0.39$ (or $\delta/H = 0.13$) at the location of the prism, considered "thin" according to the criteria of Sakamoto and Arie (1983). No-slip boundary conditions were used for the prism and ground plane surfaces, free-slip boundary conditions were used for the top and lateral boundaries and a convective outflow condition was imposed at the boundary downstream of the prism. The hexahedral grid had 2 110 336 elements, with 40 elements along each of the horizontal edges of the prism and 86 elements along its height. A slice of the grid normal to the *z* axis is illustrated in Fig. 2b. The grid was refined near the prism and ground plane surfaces to ensure that the first wall-normal elements had $y^+ < 1$. In addition, adequate grid resolution was verified based on the ratio of the subgrid-scale viscosity and the fluid viscosity (ν_{SGS}/ν) and ratio of the cubic root of the grid cell volume Δ and the estimated Kolmogorov length scale $\eta = (\nu^3/\varepsilon)^{1/4}$ (Pope, 2000) (Δ/η). The maximum values found in the time-averaged wake were of $\nu_{SGS}/\nu = 0.4$ and $\Delta/\eta = 3.8$, confirming that the majority of the flow scales were resolved.

The simulation was carried out using the pisoFoam solver of OpenFOAM v6. The central-differencing scheme was used in the spatial discretization of both advective and gradient terms, and a second-order implicit scheme was used for time. The time step was fixed at 2×10^{-5} s, which kept the values of the Courant-Friedrichs-Lewy (CFL) number below 0.3. After the flow was observed to be fully developed, 1000 time samples or snapshots were collected for a period of approximately 20 vortex shedding cycles.

In addition to the time average, a phase average analysis was performed, based on the triple decomposition of Reynolds and Hussain (1972) for periodic flows. In this approach, a fluctuating signal or flow field *u* may be decomposed into a time average contribution *U*, a periodic fluctuation $\tilde{u}$ and a turbulent fluctuation u':

$$u = U + \tilde{u} + u'. \tag{1}$$

The phase-averaged field $\langle u \rangle$ is defined as the ensemble average over a large number of samples which have the same phase as a reference signal, or:

$$\langle u \rangle = U + \tilde{u}. \tag{2}$$

During the time-averaging, the force coefficients of the prism were also recorded and the lift coefficient history was used as the reference signal to delimit the extent and phases of each vortex shedding period. Figure 3a presents the lift coefficient C_L versus the simulation flow time *t* normalized by the mean vortex shedding period $T = 1/f$, where *f* is the vortex shedding frequency. This frequency was obtained from the fast Fourier transform of the lift coefficient history (Fig. 3b), and it corresponds to a Strouhal number $St = f D/U_\infty = 0.115$. Although other peaks with St = 0.025 and 1.56 are present in the spectrum, the peak with St = 0.115 agrees with the average value of 0.11 reported in the literature (Saha, 2013; McClean and Sumner, 2014; Zhang *et al.*, 2017), and corresponds to the large-scale vortex shedding periodicity.

The periods in the lift coefficient history were identified based on the inflexion points in C_L, but only the ones that were close to the mean period *T* within a chosen tolerance of 30% were considered for the ensemble average. Each period was then discretized into 20 phase bins, following the procedure used by Bourgeois *et al*. (2011). The velocity field samples which occurred within the time intervals of a given phase bin were collected and ensemble-averaged for all periods, yielding 20 phase-averaged flow fields.

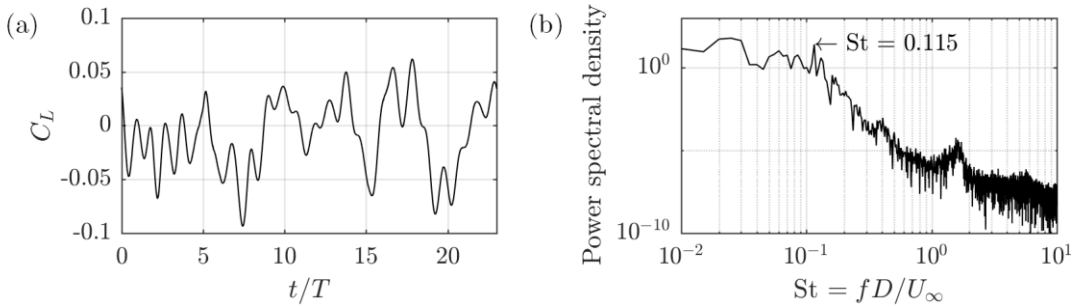

Figure 3. (a) History and (b) spectrum of the lift coefficient of the surface-mounted finite-height square prism.

3. RESULTS AND DISCUSSION

In this section, the mean flow field around the surface-mounted finite-height square prism will first be introduced, for comparison with the flow described in other studies under similar flow conditions. The phase-averaged features of the flow will then be addressed.

3.1 Mean flow field

Figure 4 presents mean velocity contours and streamlines in the *x*-*z* symmetry plane, where the region of reverse flow in the near wake and some of the critical points are highlighted. The flow field is very similar to the one obtained in the DNS of Zhang *et al*. (2017) for the same Re = 500 but for AR = 4. Vortices Bt and Nw, following the nomenclature of Sumner et al. (2017) and Krajnović (2011), are present in the upper and lower parts of the near wake, respectively. While vortex Bt is a common feature in the mean wake of surface-mounted finite-height square prisms, vortex Nw is present in the wake of prisms above the critical AR (Sumner *et al*., 2017). The horseshoe vortex can also be spotted upstream of the surface-mounted prism, at a similar location to Zhang *et al*. (2017) and da Silva *et al*. (2020).

The mid-height recirculation length, defined here as the distance between the center of the prism to the last point where the mean streamwise velocity component is equal to zero, is also illustrated in the figure. The present mean length of L_r/D = 5.5 is close to the ones obtained by Zhang *et al*. (2017) ($L_r/D \approx 6$, AR = 4, Re = 500) and Saha (2013) ($L_r/D \approx$ 6.5, AR = 3, Re = 250), but larger than the recirculation length obtained in da Silva *et al*. (2020) (L_r/D = 3.52, AR = 3, Re = 500), where a different subgrid-scale model was used. The maximum recirculation length, denoted by the reattachment point of the wake in Fig. 4, compares the same way with these other studies. The large reattachment length and the absence of a saddle point in the symmetry plane velocity streamlines are characteristics of a wake dominated by downwash, without an upwash region as obtained by Zhang *et al*. (2017) for smaller δ/D.

The mean streamwise vorticity $\omega_x D/U_\infty$ is shown in Fig. 5 in *y*-*z* planes located downstream of the prism at *x*/*D* = 4, 6.5 and 10, with the mean velocity vector field parallel to the planes included. Downwash is visible in the upper part of the wake for all planes, with a strength that correlates with the strength of the pair of streamwise vorticity regions. These vorticity regions show the typical counter-clockwise sense of rotation at the +*y* side and clockwise sense of rotation at the -*y* side of the wake. Although additional vorticity regions are present in the lower part of the wake, the flow upwash is not significant to generate stable "base vortices" and the wake is a dipole type. This is confirmed by the second invariant

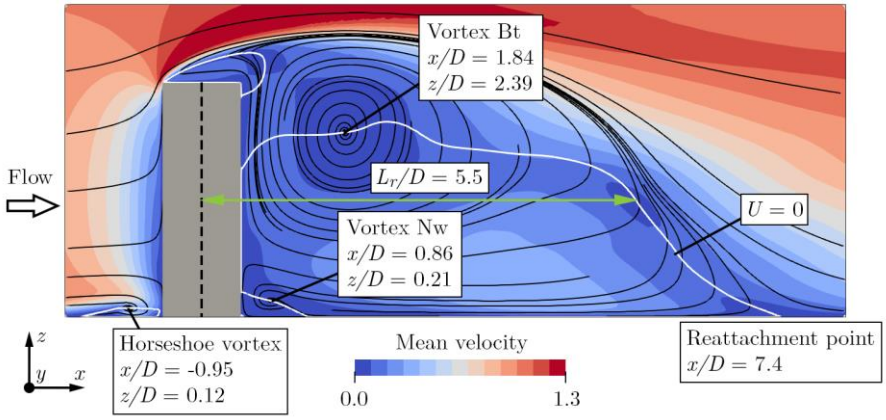

Figure 4. Contours and streamlines of the mean flow velocity normalized by U_∞ in the *x*-*z* symmetry plane. The white contour line indicates where the mean streamwise velocity component *U* is equal to zero.

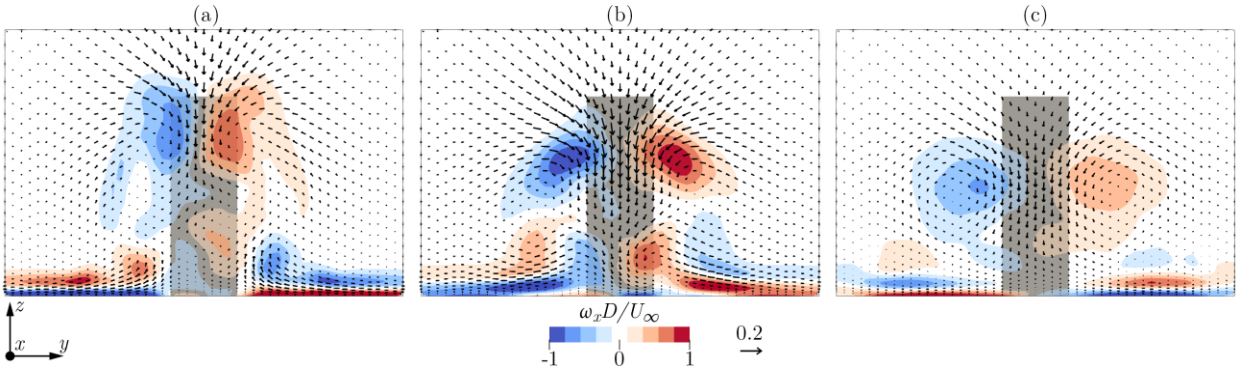

Figure 5. Contours of the mean streamwise vorticity and mean velocity vector field parallel to *y*-*z* planes located at (a) *x*/*D* = 4, (b) *x*/*D* = 6.5 and (c) *x*/*D* = 10. Every third vector is shown in the *y* and *z* directions.

of the velocity gradient tensor QD^2/U_∞^2 = 0.01 in Fig. 6, which shows prolonged tubes dominated by the streamwise vorticity that go into the far wake region.

The shape and progression of the large mean streamwise vorticity regions in the *x* direction agrees with the results of Zhang *et al.* (2017). They are positioned higher in the wake at *x*/*D* = 4, which is located inside the near-wake recirculation region, and have a side extension which was also reported by Kindree *et al.* (2018) for the high-Re wake of an AR = 4 prism. The large vorticity regions move downward downstream, increasing in size and reaching their highest magnitude at about *x*/*D* = 6.5, which is just outside the near-wake region in agreement with da Silva *et al.* (2020). Their size increases at *x*/*D* = 10, but the overall magnitude of the streamwise vorticity decreases.

The large upper vorticity regions originate from the bending of the flow that encircles the near wake by the downwash, as explained in da Silva *et al.* (2020), but the other streamwise vorticity regions in Fig. 5 have different sources. The very near-ground flow presents streamwise vorticity related to the inward flow in the near wake, and it transitions into an outward flow at *x*/*D* = 6.5 and 10 associated with the expansion of the mean wake in the *y* direction, downstream. Other streamwise vorticity regions of low magnitude are induced by this near-ground flow, but at *x*/*D* = 4 and 6.5 there are minor regions of strong vorticity that are generated from the entrainment of fluid into the wake. This mechanism is related to the bottom section of the near wake described in da Silva *et al.* (2020). This flow was also observed in other studies for different aspect ratios and flow conditions (Shah and Ferziger, 1997; Sau *et al.*, 2003; El Hassan *et al.*, 2015), with the entrainment mechanism closer to the prism having been attributed to the interaction between the wake and the horseshoe vortex. Note that the cores of the trailing arms of the horseshoe vortex are not observed in the *y*-*z* plane with *x*/*D* = 4 in Fig. 5a, which suggests that it has weakened significantly at this location possibly due to the thin boundary layer.

Overall, the time-averaged flow field presents a behavior consistent with the one reported in other studies, validating a qualitative analysis of the features of the phase-averaged flow.

3.2 Phase-averaged flow field

The phase-averaged flow around the surface-mounted finite-height square prism is presented in Fig. 7 through isosurfaces of the second invariant of the phase-averaged velocity gradient tensor ($\langle Q \rangle D^2/U_\infty^2$ = 0.1), colored by the

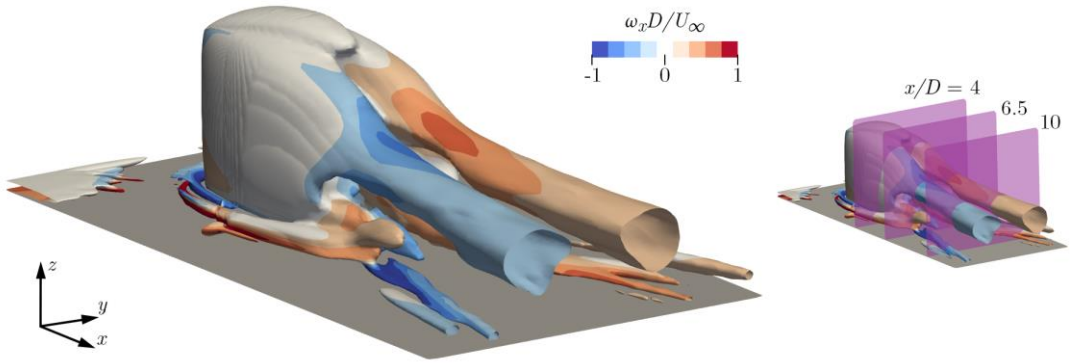

Figure 6. Isosurface of the second invariant of the mean velocity gradient tensor QD^2/U_∞^2 = 0.01 colored by the mean streamwise vorticity, and reference for the location of the planes in Fig. 5.

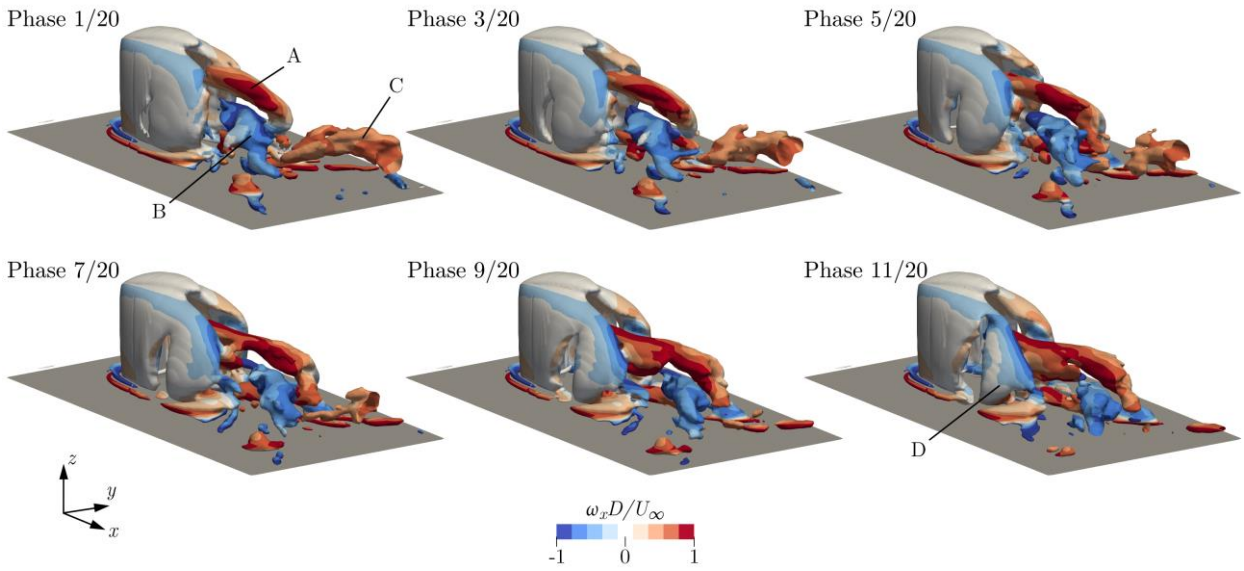

Figure 7. Isosurface of the second invariant of the phase-averaged velocity gradient tensor $\langle Q \rangle D^2/U_\infty^2$ = 0.1 colored by the phase-averaged streamwise vorticity at selected phases.

phase-averaged streamwise vorticity. The selected phases represent the progression of the phase-averaged flow for one half of the mean shedding period with St = 0.115.

The phase-averaged flow structures in Fig. 7 resemble the half-loops described by Bourgeois *et al.* (2011), but the vertical legs are only well-defined in the near wake region. The far wake is dominated by the streamwise strands of the structures, which are formed close to the middle of the wake and expand outward as they are convected downstream. Phases 1–11 show the shedding process of a structure A with positive streamwise vorticity at the +*y* side of the wake. Two additional structures which were "previously" shed are also visible: structure B with negative streamwise vorticity and structure C with positive streamwise vorticity, which corresponds to A in this phase-averaged period. At phase 11 a structure D, which corresponds to B, is shed still with its vertical leg. More details about these vorticity distributions are presented in Fig. 8 in the *y*-*z* planes with *x*/*D* = 4, 6.5 and 10, which represent the near-wake, transition and far-wake regions, respectively.

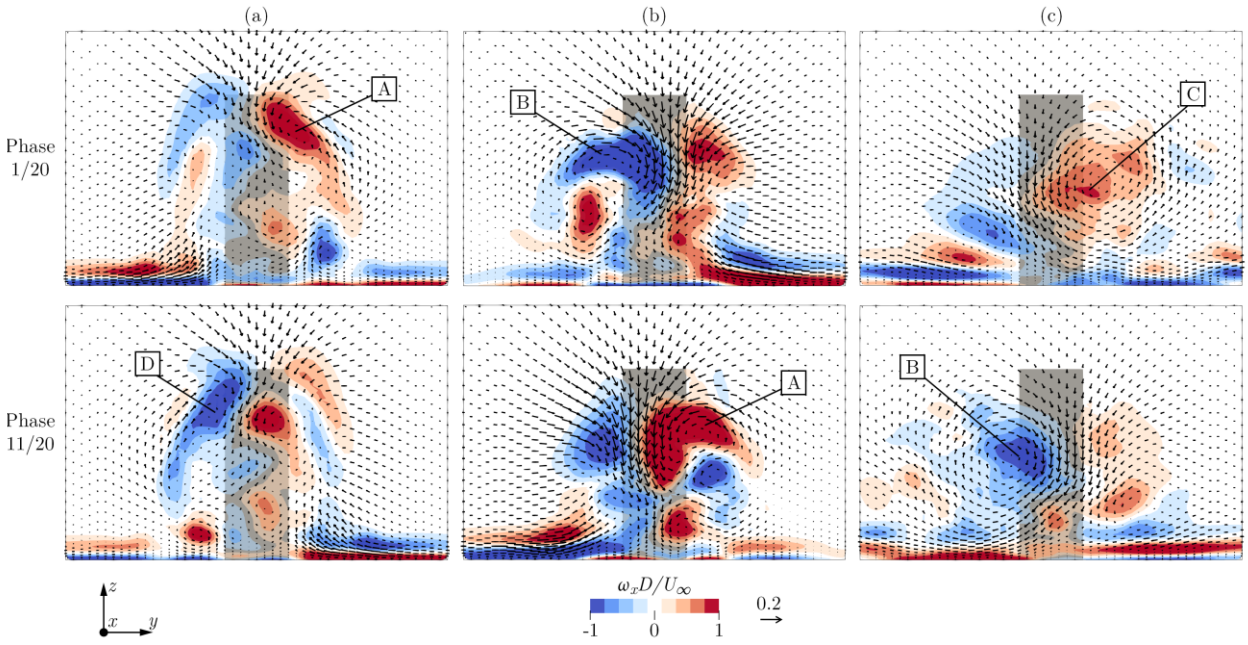

Figure 8. Contours of the phase-averaged streamwise vorticity and velocity vector field parallel to *y*-*z* planes located at (a) *x*/*D* = 4, (b) *x*/*D* = 6.5 and (c) *x*/*D* = 10 for phases 1/20 and 11/20. Every third vector is shown in the *y* and *z* directions.

The large vorticity regions in the upper part of the wake in Fig. 8 follow the same patterns of the time-averaged vorticity in Fig. 5, regarding changes along *x/D*. The phases 1/20 and 11/20, which are opposite to each other, show that the vorticity alternates in strength between the sides of the wake following the structures of Fig. 7. For example, at *x/D* = 6.5 (Fig. 8b), structure B occupies the *-y* side of the wake at phase 1/20 while structure A is stronger at the *+y* side at phase 11/20. The fluid entrainment caused by the downwash follows this alternate behavior, as shown by the phased-averaged velocity vector fields. Streamlines of the phase-averaged velocity field are presented in Fig. 9a for the same phases as Fig. 8, located at the upper part of the wake (seed points at *x/D* = -0.17, *y/D* = ±0.2, *z/D* = 0.67–1). They confirm the association of the downwash-induced fluid entrainment with the structures' streamwise strands and reveal a large-scale motion of the phase-averaged wake in the transverse direction. In addition, the flow in the near wake by the top of the prism (*z/D* = 3) is shown to be more symmetric, in agreement with the reports of Wang and Zhou (2009), Sattari *et al.* (2012) and Behera and Saha (2019) and in contrast with the flow in the bottom section of the wake in Fig. 9b.

The phase-averaged flow in the bottom part of the wake has a more complex behavior. At *x/D* = 4 (Fig. 8a), an additional streamwise vorticity region of high intensity is found at the same side of the major upper vorticity, but with opposite sense of rotation, near the ground plane. It resembles the base vortex of a full-loop structure (Hosseini *et al.*, 2013), which is typically found for thicker boundary layers, and may be related to the presence of vortex Nw in Fig. 4. This vorticity distribution and the shape of the structures in Fig. 7 suggest that the shed structures have initially a full-loop shape, but they are molded into the streamwise strands downstream by the downwash and the surrounding flow.

At *x/D* = 6.5 (Fig. 8b), the streamwise vorticity distribution is connected to the alternate fluid entrainment mechanism close to the ground plane. The streamlines in Fig. 9b were seeded at *x/D* = -0.17, *y/D* = ±0.25 and *z/D* = 0–0.2 to illustrate this mechanism. Note that the main horseshoe vortex has significant strength only in the very-near-wake region, but its induced vorticity of opposite sense of rotation extends into the near wake from the *-y* side at phase 1/20, causing the strong positive (counter-clockwise) vorticity at this side which is also visible at *x/D* = 4 (Fig. 8a). Some of the streamlines ascend inside the near wake region, following the same mechanism described in da Silva *et al.* (2020), while others encircle structures A and B. On the other side of the wake at phase 1/20, fluid entrainment still occurs but it is more subtle and bypasses the near wake recirculation region. At phase 11/20, the described mechanisms shift sides, causing stronger vorticity concentrations near the ground plane at the *+y* side of the wake.

The upper phase-averaged streamwise vorticity regions are, overall, less intense at *x/D* = 10 (Fig. 8c) due to the dissipation of the flow structures in the far wake. Additional low-magnitude vorticity regions are, still, alternately induced by the interaction of the vorticity near the ground plane and the flow structures, following the large-scale transverse movement of the wake.

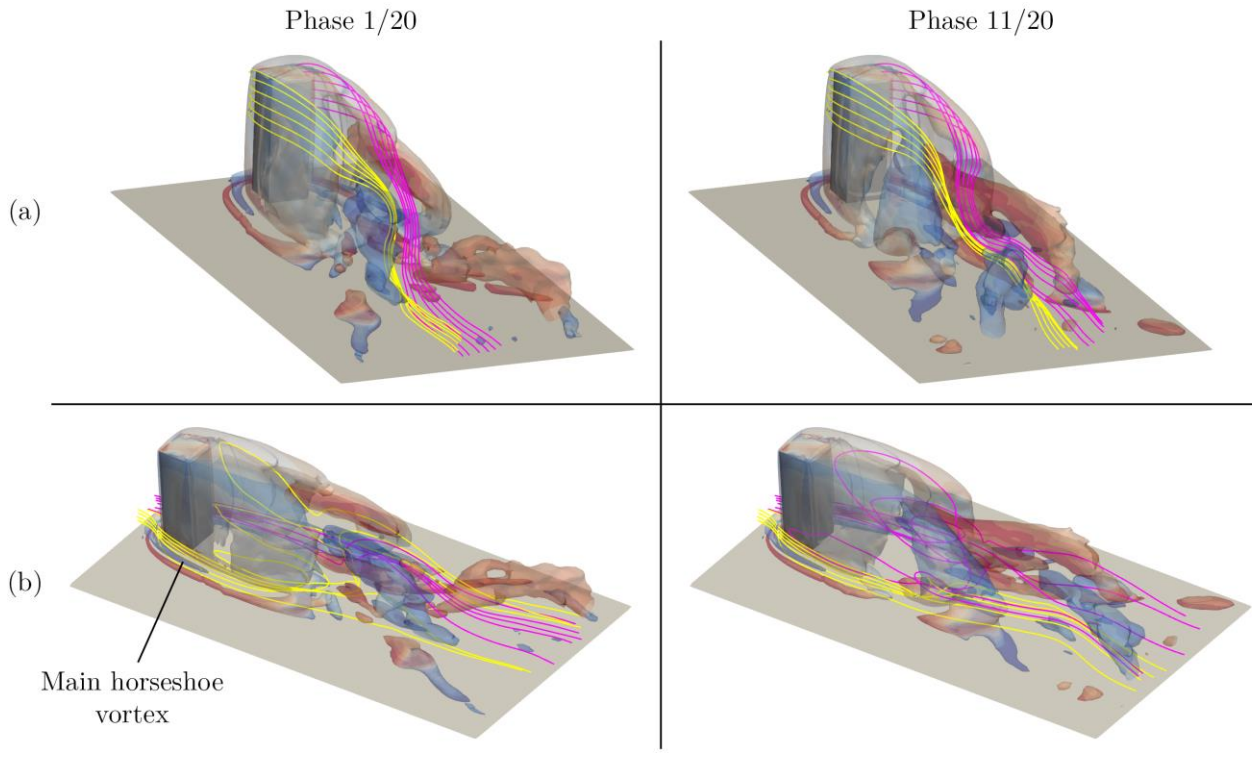

Figure 9. Representative streamlines of the flow at the (a) top and (b) bottom sections of the phase-averaged wake, overlapped with the semi-transparent isosurfaces of Fig. 7 for phases 1/20 and 11/20. Streamlines originating at the *-y* and *+y* sides of the domain are colored yellow and magenta, respectively.

4. CONCLUSIONS

The flow around a surface-mounted finite-height square prism with AR = 3, Re = 500 and δ/D = 0.39 was investigated based on large-eddy simulation results. An analysis of the time-averaged flow field served as a means to provide qualitative validation, by comparing several of its elements like the mean wake recirculation length and streamwise vorticity distribution with published studies of this type of flow.

The dynamic wake of the surface-mounted finite-height square prism was investigated based on the phase-averaged flow field. Alternate flow structures similar to the half-loops of Bourgeois *et al.* (2011) were found, but with two major differences for the present flow conditions. First, despite the thin boundary layer, the structures consisted more of full-loops in their formation, with the base vorticity disappearing outside the near wake. Second, the far wake was dominated by the streamwise strands of these structures, due to the downwash-induced entrainment of the surrounding fluid in the upper region, which caused a large-scale alternating motion of the wake in the transverse direction.

The phase-averaged flow near the top of the prism in the near wake had a more symmetric behavior, but an antisymmetric fluid entrainment mechanism was found in the bottom section of the wake, near the ground plane. This mechanism was not caused directly by the main horseshoe vortex, but by the fluid nearby it. It took place simultaneously on both sides of the wake, although in different ways depending on the arrangement of the phase-averaged flow structures.

5. ACKNOWLEDGEMENTS

Financial support from the National Sciences and Engineering Research Council of Canada (NSERC) Discovery Grants program and the University of Saskatchewan's Dean's Scholarship program is gratefully acknowledged.

6. REFERENCES

Behera, S. and Saha, A.K., 2019. “Characteristics of the flow past a wall-mounted finite-length square cylinder at low Reynolds number with varying boundary layer thickness”. *Journal of Fluids Engineering*, Vol. 141, p. 061204.

Bourgeois, J.A., Sattari, P. and Martinuzzi, R.J., 2011. “Alternating half-loop shedding in the turbulent wake of a finite surface-mounted square cylinder with a thin boundary layer”. *Physics of Fluids*, Vol. 23, p. 095101.

Da Silva, B.L., Chakravarty, R., Sumner, D. and Bergstrom, D.J., 2020. “Aerodynamic forces and three-dimensional flow structures in the mean wake of a surface-mounted finite-height square prism”. *International Journal of Heat and Fluid Flow*, Vol. 83, p. 108569.

El Hassan, M., Bourgeois, J. and Martinuzzi, R., 2015. “Boundary layer effect on the vortex shedding of wall-mounted rectangular cylinder”. *Experiments in Fluids*, Vol. 56, p. 33.

Hosseini, Z., Bourgeois, J.A. and Martinuzzi, R.J., 2013. “Large-scale structures in dipole and quadrupole wakes of a wall-mounted finite rectangular cylinder”. *Experiments in Fluids*, Vol. 54, p. 1595.

Igarashi, T., 1984. “Characteristics of the flow around a square prism”. *Bulletin of the JSME*, Vol. 27, p. 1858–1865.

Kawai, H., Okuda, Y. and Ohashi, M., 2012. “Near wake structure behind a 3D square prism with the aspect ratio of 2.7 in a shallow boundary layer flow”. *Journal of Wind Engineering and Industrial Aerodynamics*, Vol. 104–106, p. 196–202.

Kindree, M.G., Shahroodi, M. and Martinuzzi, R.J., 2018. “Low-frequency dynamics in the turbulent wake of cantilevered square and circular cylinders protruding a thin laminar boundary layer”. *Experiments in Fluids*, Vol. 59, p. 186.

Krajnović, S., 2011. “Flow around a tall finite cylinder explored by large eddy simulation”. *Journal of Fluid Mechanics*, Vol. 676, p. 294–317.

McClean, J.F. and Sumner, D., 2014. “An experimental investigation of aspect ratio and incidence angle effects for the flow around surface-mounted finite-height square prisms”. *Journal of Fluids Engineering*, Vol. 136, p. 081206.

Meneveau, C., Lund, T.S. and Cabot, W.H., 1996. “A Lagrangian dynamic subgrid-scale model of turbulence”. *Journal of Fluid Mechanics*, Vol. 319, p. 353–385.

Ozgoren, M., 2006. “Flow structure in the downstream of square and circular cylinders”. *Flow Measurement and Instrumentation*, Vol. 17, p. 225–235.

Pope, S.B., 2000. *Turbulent flows*. Cambridge University Press, Cambridge, UK.

Porteous, R., Moreau, D.J. and Doolan, C.J., 2017. “The aeroacoustics of finite wall-mounted square cylinders”. *Journal of Fluid Mechanics* Vol. 832, p. 287–328.

Reynolds, W.C. and Hussain, A.K.M.F., 1972. “The mechanics of an organized wave in turbulent shear flow. Part 3. Theoretical models and comparisons with experiments”. *Journal of Fluid Mechanics*, Vol. 54, p. 263–288.

Saha, A.K., 2013. “Unsteady flow past a finite square cylinder mounted on a wall at low Reynolds number”. *Computers & Fluids*, Vol. 88, p. 599–615.

Sakamoto, H. and Arie, M., 1983. “Vortex shedding from a rectangular prism and a circular cylinder placed vertically in a turbulent boundary layer”. *Journal of Fluid Mechanics*, Vol. 126, p. 147–165.

Sattari, P., Bourgeois, J.A. and Martinuzzi, R.J., 2012. “On the vortex dynamics in the wake of a finite surface-mounted square cylinder”. *Experiments in Fluids*, Vol. 52, p. 1149–1167.

Sau, A., Hwang, R.R., Sheu, T.W.H. and Yang, W.C., 2003. “Interaction of trailing vortices in the wake of a wall-mounted rectangular cylinder”. *Physical Review E*, Vol. 68, p. 056303.

Shah, K.B. and Ferziger J.H., 1997. “A fluid mechanicians view of wind engineering: Large eddy simulation of flow past a cubic obstacle”. *Journal of Wind Engineering and Industrial Aerodynamics*, Vol. 67–68, p. 211–224.

Sumner, D., Rostamy, N., Bergstrom, D.J. and Bugg, J.D., 2017. “Influence of aspect ratio on the mean flow field of a surface-mounted finite-height square prism”. *International Journal of Heat and Fluid Flow*, Vol. 65, p. 1–20.

Wang, H.F., Zhou, Y., Chan, C.K., Wong, W.O. and Lam, K.S., 2004. “Flow structure around a finite-length square prism”. In: *Proceedings of the 15th Australasian Fluid Mechanics Conference*. Sydney, Australia, December 13-17, 2004.

Wang, H.F. and Zhou, Y., 2009. “The finite-length square cylinder near wake”. *Journal of Fluid Mechanics*, Vol. 638, p. 453–490.

Yauwenas, Y., Porteous, R., Moreau, D.J. and Doolan, C.J., 2019. “The effect of aspect ratio on the wake structure of finite wall-mounted square cylinders”. *Journal of Fluid Mechanics*, Vol. 875, p. 929–960.

Zhang, D., Cheng, L., An, H. and Zhao, M., 2017. “Direct numerical simulation of flow around a surface-mounted finite square cylinder at low Reynolds numbers”. *Physics of Fluids*, Vol. 29, p. 045101.

Zu, G. and Lam, K.M., 2018. “Simultaneous measurement of wind velocity field and wind forces on a square tall building”. *Advances in Structural Engineering*, Vol. 21, p. 2241–2258.

7. RESPONSIBILITY NOTICE

The authors are the only responsible for the printed material included in this paper.